Single-junction organic solar cells with over 19% efficiency enabled by a refined double-fibril network morphology

Lei Zhu[1,8], Ming Zhang[1,8], Jinqiu Xu[1,8], Chao Li[2], Jun Yan[3]*, Guanqing Zhou[1], Wenkai Zhong[1], Tianyu Hao[1], Jiali Song[2], Xiaonan Xue[1], Zichun Zhou[1], Rui Zeng[1], Haiming Zhu[4], Chun-Chao Chen[5], Roderick C.I. MacKenzie[6], Yecheng Zou[7], Jenny Nelson[3], Yongming Zhang[1,7], Yanming Sun[2]*, Feng Liu[1,7]*

[1]Frontiers Science Center for Transformative Molecules, In-situ Center for Physical Science, and Center of Hydrogen Science, School of Chemistry and Chemical Engineering, Shanghai Jiao Tong University, Shanghai 200240, China.

[2]School of Chemistry, Beihang University, Beijing 100191, China.

[3]Department of Physics, Imperial College London, London SW7 2AZ, UK.

[4]Department of Chemistry, Zhejiang University, Hangzhou, Zhejiang 310027, China.

[5]School of Materials Science and Engineering, Shanghai Jiao Tong University, Shanghai 200240, China.

[6]Department of Engineering, Durham University, Durham DH1 3LE, UK.

[7]State Key Laboratory of Fluorinated Functional Membrane Materials and Dongyue Future Hydrogen Energy Materials Company, Zibo, Shandong 256401, China.

[8]These authors contributed equally: Lei Zhu, Ming Zhang, Jinqiu Xu.

*email: j.yan17@imperial.ac.uk; sunym@buaa.edu.cn; fengliu82@sjtu.edu.cn

Abstract

In organic photovoltaics, morphological control of donor and acceptor domains on the nanoscale is key for efficient exciton diffusion and dissociation, carrier transport, and suppression of recombination losses. To realise this, here, we demonstrated a double-fibril network based on ternary donor:acceptor morphology with multi-length scales constructed by combining ancillary conjugated polymer crystallizers and non-fullerene acceptor filament assembly. Using this approach, we achieved an average power conversion efficiency of 19.3% (certified 19.2%). The success lies in the good match between the photoelectric parameters and the morphological characteristic lengths, which utilizes the excitons and free charges efficiently. This strategy leads to enhanced exciton diffusion length (hence exciton dissociation yield) and reduced recombination rate, hence minimizing photon-to-electron losses in the ternary devices as compared to their binary counterparts. The double-fibril network morphology strategy minimizes losses and maximizes the power output, offering the possibility towards 20% power conversion efficiencies in single-junction organic photovoltaics.

Main

Organic semiconductors offer the advantage of high optical absorption and tunable energy levels, enabling thin-film solar cells with high light-to-electron conversion efficiencies over a wide range of wavelengths[1-4]. Desipte recent progresses, the performance of organic solar cells (OSCs) is still limited by non-ideal exciton and charge transport, which depend not only on the electronic structure of organic semiconductors but also on the nanostructure that is formed by material crystallization and phase separation in a bulk heterojunction (BHJ) setting[5-8]. A suitable sized phase-separated morphology that balances crystalline region and mixing domain on the nanoscale is therefore needed to further push the power conversion efficiency (PCE) of OSCs, however it is a

nontrivial endeavor since the thin-film deposition is a non-equilibrium process that depends on multiple factors including the chemical structures and processing conditions[9].

A useful strategy to manipulate thin-film morphology is the introduction of a third component which can selectively interact with donor or acceptor to induce extra morphology control handles[6,10-15]. And by using enthalpy dictated crystallization, a crystallization induced phase-separated morphology with suitable size scale can be achieved[16,17], creating an intertwined donor (D)-acceptor (A) bicontinuous network with domains on the tens of nanometers scale, such that efficient exciton and carrier transport can be achieved. Meanwhile, the size of the mixing domain needs to be refined to enhance the carrier diffusion before on board the crystalline transport phase, which dictates the efficiency of carrier transport at conditions close to open circuit, hence influencing the fill factor (FF) of the device.

In this work, a bicontinuous double-fibril network morphology (DFNM) is demonstrated using a carefully designed ternary mixture, in which the phase separation, crystallinity, and specific fibril widths are collectively manipulated. The resulting nanostructure matches well with the requirements for efficient exciton and free charge transport with ~40 nm exciton diffusion length, ~105 nm free charge diffusion length, and ~2700 nm free charge drift length (estimated at short circuit condition)[18,19]. The matured crystallization of polymer donor and non-fullerene acceptor (NFA) fibrils in the blended thin film leads to a reduced mixing zone and suppressed recombination. An extraordinary FF of ~82% is recorded and a breakthrough in average PCE of 19.3% with a maximum value of 19.6% is obtained in the optimized single-junction OSCs. Similar improvements are seen in parallel experiments with a similar morphology, showing the bright future of the DFNM perspective.

Materials and device performance

The chemical structure and absorption spectra of materials used in this research are shown in Fig. 1a and Supplementary Fig. 1. L8-BO primarily absorbs light between 550 and 900 nm[20]. PM6 and D18 in combination are used as donors to absorb short-wavelength photons from 400–700 nm and to manipulate material crystallization forming a high-quality crystalline donor phase. The highest occupied molecular orbital (HOMO) and lowest unoccupied molecular orbital (LUMO) energies are –5.20 eV/–3.06 eV for PM6, –5.24 eV/–2.95 eV for D18, and –5.67 eV/–3.92 eV for L8-BO measured by ultraviolet photoelectron spectroscopy (UPS) and inverse photoemission spectroscopy (IPES)[21], respectively (Fig. 1b and Supplementary Fig. 2). The current density–voltage (*J*–*V*) curves and performance parameters of the devices are shown in Fig. 1c, Supplementary Fig. 3, and Table 1. The device based on PM6:L8-BO achieved a maximum PCE of 18.2% with an open-circuit voltage (V_{oc}) of 0.888 V, a short-circuit current density (J_{sc}) of 25.7 mA cm^{-2}, and a FF of 79.9%, while D18:L8-BO showed a V_{oc} of 0.907 V, a J_{sc} of 24.9 mA cm^{-2}, a FF of 78.5%, and a PCE of 17.7%. The best mixing weight ratio of PM6:D18:L8-BO=0.8:0.2:1.2 offers a maximum PCE of 19.6% with a V_{oc} of 0.896 V, a J_{sc} of 26.7 mA cm^{-2}, and a FF of 81.9%. Such device obtained a certified PCE of 19.2% subject to the calibration procedures of the National Photovoltaic Industry Metrology and Testing Center (NPVM, China, Supplementary Fig. 4), which is a breakthrough from the previous record[4,22-25]. The highly crystalline polymer D18 is used as the seeding agent for the moderate crystalline polymer PM6 in order to retain the advantageous PM6:L8-BO morphology framework while enhancing the crystallinity of the blend[20,26]. An optimum amount of D18 added into PM6:L8-BO raises J_{sc} and FF simultaneously (Fig. 1d, Supplementary Fig. 5a and Supplementary Table 1), Meanwhile, the glass-encapsulated devices exhibited ~95% of the initial PCE after 2520 hours of storage in the glove box at 25 ℃. More importantly, the ternary device showed better

illumination stability than that of binary devices, indicating that the introduction of D18 can better balance the photochemical and morphology stability of the blend system (shown in Supplementary Fig. 6). The external/internal quantum efficiency (EQE/IQE) results show an increase in EQE of the ternary device due to more efficient exciton diffusion, which contributes to improved J_{sc} and PCE (see Fig. 1e, Supplementary Figs. 5b,c and 7, and Supplementary Note 1 for details.) The statistics of solar cell devices were shown in Fig. 1f and a jump in PCE value is recorded in the ternary mixture.

Morphology details of double-fibril network

To understand the origin of the encouraging device performance, we investigated the film microstructure. As shown by transmission electron microscopy (TEM) investigation (Fig. 2a and Supplementary Fig. 8), a fibrillar network structure is seen in all blended films. The fibril texture in primitive PM6:L8-BO blends is roughly defined with a smaller fibril diameter and more sparse fibril distribution. D18 is a strongly crystalline polymer and of slightly low solubility than PM6, which precipitate out in an earlier film growth stage and induce crystallization. Adding D18 into PM6 helps to improve the crystallinity of the blends by forming a high-quality fibril network with increased fibril diameter and distribution, as evidenced by atomic force microscope (AFM) and scanning electron microscope (SEM) characterizations (Supplementary Figs. 9 and 10). The Fourier transformation yields an inter-fibril distance ~25 nm, a suitable length scale of phase separation to balance exciton splitting and carrier transport. With this phase image, we then looked into the detailed phase construction of the blended thin-films. Photo-induced force microscope (PiFM) was employed that uses localized near field infrared imaging to identify the chemistry associated with thin-film morphology (see Fig. 2b, Supplementary Figs. 11 and 12, and Supplementary Note 2 for details). The corresponding PiFM phase images of

PM6:D18:L8-BO blends were shown in Fig. 2b and Supplementary Fig. 12a. Interestingly, both PM6 and L8-BO formed fibril network structures in the blend. The overlay of the two images (Supplementary Fig. 12b) yields an entangled DFNM with donor and acceptor domain in close contact. Such observation provides a good understanding of the OSCs' morphology, indicating that crystallization-induced morphology can result in better phase connectivity and finer sizes. Line profiles across PiFM images were shown in Fig. 2b, full width at half maximum (FWHM) of the peaks was used to estimate the fibril diameter, yielding average values of 22.1 and 22.6 nm for acceptor and donor fibrils. In combination with the inter fibril distance value, it can be concluded that the mixing domain volume is low, indicating low geminate recombination and high FF as discussed later in more detail.

Grazing incidence X-ray diffraction (GIXD) was used to investigate the thin film crystallinity[27]. The 2D diffraction patterns and 1D line cuts are summarized in Fig. 2c,d and Supplementary Fig. 13a–c. Both donor and acceptor show good crystalline order in neat films (show in Supplementary Fig. 13a and Supplementary note 3). In blended films, both conjugated polymers and NFA are preferentially face-on oriented according to π–π stacking peak locations, which facilitate carrier transport. The overlapping of lamellar and π–π stacking peaks were used to evaluate the structure order of the thin film (shown in Supplementary Fig. 14 and Supplementary Table 2). The D18:L8-BO film exhibits high crystallinity and large crystal size, where the PM6:L8-BO film shows weak crystallinity and small crystal size, and the PM6:D18:L8-BO film lies in-between and is close to PM6:L8-BO film. The (021) diffraction peak in L8-BO was used to label the NFA crystallization feature in blends (Supplementary Figs. 13d,e and 15 and Supplementary Table 3). It is found that D18 retains a good crystallinity in ternary blends as evidenced by its (001) diffraction intensity and crystal coherence length (CCL).

D18's presence also promotes the crystallization of L8-BO, judging from its (021) peak area enhancement. The small amount of D18 in ternary blend promotes the crystallization of both donor polymer and NFA molecules. We ascribe such effect to the heterogeneous nucleation seeding mechanism[28,29], which helps to increase the fibril content and crystallite quality in a blended thin-film.

Resonant soft X-ray scattering (RSoXS) is used to investigate the phase separation at the energy of 285.2 and 286.7 eV related to C 1s → π* transition (see Supplementary Figs. 16 and 17, and Supplementary Note 4 for details) by taking advantage of energy-dependent chemical sensitivity[30-34]. The D18:L8-BO blends show a broad scattering hump with the center around 0.0098 $Å^{-1}$ (64.1 nm) at both photon energy (Supplementary Fig. 17a), where the PM6:L8-BO blends show a better-resolved scattering hump at 285.2 eV located at 0.0131 $Å^{-1}$ (47.8 nm) (Supplementary Fig. 17b). Introducing D18 into PM6:L8-BO leads to the enhancement of RSoXS with a slightly reduced hump center (q = 0.0130 $Å^{-1}$, 48.2 nm) (Supplementary Fig. 17c). NK-NEXAFS was conducted to further clarify the chemical origin of the contrast (as shown in Supplementary Fig. 17d). From the NK-NEXAFS of the nitrogen-containing material D18 and L8-BO, the absorption of the blend film at 400 eV is only from L8-BO (Supplementary Fig. S16b). Therefore, the phase separation scales of L8-BO in the three blend films are 68.8 nm (D18:L8-BO), 49.0 nm (PM6:L8-BO), and 51.8 nm (PM6:D18:L8-BO), respectively, which is consistent with the result of 285.2 eV in CK-RSoXS. Thus, D18 could induce a better-defined fibril structure in ternary blends by improving the fibril diameter, as demonstrated by AFM and PiFM characterization. It is noted that the inter-fibril distance is only slightly larger than the diameter of the fibril, thus the mixing region in-between the fibrils is small (summarized in Supplementary Table 4). Therefore, the charges in the mixing zone could effectively diffuse to

the fibril network and be collected by electrodes. Scattering anisotropy is seen in RSoXS (Supplementary Fig. 17), which is parallel with a polarized electrical field at 285.2 eV. Thus, the L8-BO fibril/mixing zone interface is "edge-on" oriented[35,36]. A schematic illustration of this DFNM is shown in Fig. 2e. The closely packed D-A fibrils in the mixture matrix enjoy an efficient exciton splitting and carrier transport, as will be shown later.

Exciton diffusion and photophysical analysis

To further clarify the the exciton diffusion properties in the films based on the optimized DFNM, we carried out exciton annihilation method to measure exciton diffusion constants (see Supplementary Table 5 and Supplementary Note 5 for details). The results show that the addition of D18 to PM6:L8-BO increased the exciton diffusion length in the donor phase by ~11%, steming from the optimized morphology with increased in fibril crystallinity and diameter.

Next, we carried out transient absorption spectroscopy (TAS) measurements to look into the exciton and carrier dynamics within DFNM (see Supplementary Figs. 18–21, and Supplementary Note 6 for details)[37,38]. In blended films (Supplementary Figs. 19–21) with the decay of L8-BO bleach and stimulated emission (SE) peak at ~840 nm, D18 bleach peak in 550–650 nm rises, indicating the hole transfer process. The kinetics of 600 nm in three blends are extracted (Supplementary Fig. 22) and fitted with a double exponential decay function (Supplementary Table 6). The hole transfer in PM6:L8-BO is faster compared to D18:L8-BO (smaller τ_1 value), and exciton diffusion time is longer in D18:L8-BO compared to PM6:L8-BO (larger τ_2 value). Such observation implies the differences in morphology, in which PM6:L8-BO forms a good mixing zone and D18:L8-BO has a larger NFA fibril diameter. The ternary blends show a τ_1 value close to that of PM6:L8-BO and a τ_2 value close to that of D18:L8-BO. Thus, the

advantages of the two binary blends are naturally collected in the ternary blend, leading to superior performance in J_{sc} and FF. The kinetics of the polaron state was shown in Supplementary Fig. 23. The ternary blend film shows the slowest decay, originating from the improved morphology that surpresses recombination.

Device physics

The photocurrent (J_{ph}) as a function of effective voltage shows the ternary blends have a higher capability in both charge generation and transport. (see Supplementary Fig. 24, Supplementary Table 7 and Supplementary Note 7 for details). The charge transport properties are further evaluated through space charge limited current (SCLC) method, as shown in Supplementary Fig. 25 and Supplementary Tables 8 and 9. Both hole and electron mobilities are on the order of 10^{-3} cm^2 V^{-1} s^{-1}. For PM6:L8-BO devices, the lower hole mobility sets the fundamental limit, hence limiting the performance. The introduction of D18 leads to high and balanced transportation (Fig. 3a) that can reduce the likelihood of bimolecular and trap-assisted recombinations. Transient photovoltage (TPV) measurements were performed to investigate the carrier dynamics under different V_{oc} conditions[39]. As shown in Supplementary Fig. 26a, the lifetimes of the ternary devices show an enhancement in a broad operating range, indicating less free charge recombination in the ternary blends than the binaries. Combining the lifetime values with the extracted mobility values, the carrier diffusion and drift length at short circuit[18,19] can be estimated via $L_d = \sqrt{\frac{k_B T}{q}\mu\tau}$ and $L_{dr} = \frac{\mu\tau V_{bi}}{d}$, respectively (see Fig. 3b, Supplementary Table 10, and Supplementary Note 8 for details). All devices show high free charge drift length from close to 1000 nm to above 2000 nm (way above device thickness), indicating efficient charge collection at short circuit conditions and negligible loss of IQE, EQE, and J_{sc} due to free charge

collection losses. The difference between the diffusion lengths (Fig. 3b) could explain the enhanced FF in the ternary device. Moreover, in the ternary device, a balanced diffusion length of ~105 nm and drift length (at short circuit condition) of ~2700 nm are obtained, which in combination with the typical photogeneration depth, guarantees an efficient ambipolar charge transport in ternary blends. Moreover, transient photocurrent (TPC), TPV, and Mott-Schottky methods were used to probe the density of states (DoS) and recombination mechanisms. We find that the ternary device possesses the lowest recombination coefficient and the highest occupied density of states of LUMO, as shown in Fig. 3c,d, and that trap assisted recombination has limited contribution (see Supplementary Figs. 27–29, Supplementary Table 11, and Supplementary Note 9 for details).

So far, the key findings here are: i) exciton diffusion and charge generation are enhanced; ii) bimolecular recombination is suppressed; iii) charge transport is optimized; iv) high density of states is obtained in the ternary devices; and v) trap-assisted recombination is negligible in all devices, which are consistent with improved EQE, IQE, J_{sc}, and FF in the ternary devices.

Exciton diffusion, optical, and electrical simulation

To further support experimental results, we here perform quantitative device modelling, using a coupled exciton diffusion, optical transfer matrix, and drift diffusion model based on gpvdm[40-42]. Specifically, the effects of exciton diffusion efficiency and free charge recombination rate constant on IQE/EQE and FF are modelled (see Supplementary Figs. 30–32, Supplementary Tables 12–13, and Supplementary Note 10 for details). By modelling exciton diffusion within a single, spherical, acceptor domain whose size is determined by the phase separation length, and using exciton diffusion lengths from Supplementary Table 12, we demonstrate that exciton collection is more efficient from the ternary and PM6:L8-BO structures

(~97%) than from the lowest performing D18:L8-BO structure (~94%). Further simulations based on optical and electrical models also demonstrated the highest IQE/EQE, $J_{sc,}$ and FF in the ternary blends (see Supplementary Fig. 32), which is a collective effect by the efficient exciton diffusion and suppressed recombination, further supporting the claim that enhanced exciton dissociation yield and reduced free charge recombination are important reasons for the performance enhancement in the ternary device.

Formation mechanism of DFNM

While the conjugated polymer shows a high tendency to form crystalline fibrils, the NFA molecule crystallization behavior is a curious property to investigate. Conventional NFAs that rely on π–π stacking to form ordered structures have a high tendency to form 2D brick wall packing or 3D network packing[43,44]. The Y6 molecules with a banana geometry show a different packing motif whereby they align their molecular long axes to form a polymer-like structure and extend along the body center diagonal in the lattice plane[45]. The L8-BO with a long branched side-chain gives slightly stronger alkyl chain interactions and adopts a more condensed packing with the long axis along the face center half diagonal, forming smaller domains between conjugated backbones in crystals. A careful examination of the single crystal yields more interesting information in which multiple dimer packing motifs are seen (Fig. 4a–c) and 8 monomer packing is needed to form a complete period. More importantly, several linear molecular assemblies intertwined together to form a strong assembly with a high aspect ratio (Fig. 4b,c) that can be of high tolerance to local structure defects. These properties make L8-BO forming needle-type single crystals (Fig. 4d). In the TEM diffraction investigation, it is confirmed that the molecular long axis is aligned with needle packing length (Fig. 4e). Such nature is preserved to form fibrils in blended thin films (Fig. 4f).

Material selection rules for constructing DFNM

DFNM enables efficient exciton and free charge transport in the blended thin films studied herein. To confirm that, we try to correlate the fundamental photophysical properties of donor and acceptor materials in the blend with the structural features. A large group of acceptor materials was studied to look into the detailed photophysical property change versus material nature. The representative exciton decay kinetics as a function of excitation density of L8-BO is shown in Supplementary Fig. 33, from which the exciton diffusion length can be estimated. As shown in Fig 5a, Supplementary Figs. 34 and 35, and Supplementary Table 14, we see that PCBM acceptors have a low diffusion length around 5 nm, ITIC families have a diffusion length of 10–20 nm, Y6 based NFAs show a much larger diffusion length ~40 nm, which is well above the fibril diameter and should guarantee a highly efficient exciton splitting. The exciton diffusion in the donor phase is also investigated as complementary to acceptors (Fig. 5b, Supplementary Figs. 36–39, and Supplementary Table 14). The conventionally used donor materials such as PM6, PM7, and PTQ10 show an exciton diffusion length around 14 nm, which is much lower compared to that in the high-efficiency Y6 acceptor family. Thus, enhancing the exciton diffusion of polymer donors can be a viable approach in improving photo harvesting. We noticed that several high crystalline donor polymers have higher exciton diffusion lengths compared to the above-mentioned donor polymers, and thus designed the binary donor polymer blends to improve exciton diffusion. Adding a secondary, high crystalline donor (20 wt.%) such as D18 could improve the exciton diffusion length to around 20 nm, which better matches the polymer fibril's diameter and catches up with that in NFAs. We believe this property could result in better photo management in devices, leading to high J_{sc} and FF.

Last, solar cell performances in these NFA-based systems (chemical structure of materials were summarized in Supplementary Fig. 40) are used to establish the correlation between

281 photophysical features and morphological structures. As shown in Fig. 5c, Supplementary Figs.
282 41–43, and Supplementary Tables 15–17, conventional ITIC analogs using the ternary blends do
283 not help to improve device performance, and obvious FF drop is recorded in several blends. We
284 ascribe these results to unoptimized NFA morphology in which domain connection is an issue
285 (no similar fibril network channels are formed). In the Y6-based NFA blended system, the
286 ternary blends with improved exciton diffusion length and donor-acceptor crystallinity do help to
287 improve the J_{sc} and FF, resulting in higher PCEs. In addition, we ran experiments on more
288 blending ratios and different material systems to monitor the device performances and
289 characteristics (see Supplementary Figs. 44–49, Supplementary Tables 18–21, and
290 Supplementary Note 11 for details). The results show that an appropriate reduction of the mixing
291 zone size can increase exciton utilization. The high-quality double fibril transport channel
292 ensures the efficient diffusion of carriers and is no longer a shortboard that restricts the
293 performance of the device.

294 **Outlook**

295 From the above-discussed observations, the successful demonstration of adding D18 into the
296 PM6:L8-BO blends provides a showcase of average efficiency of 19.3% (certified 19.2%),
297 associated with very high J_{sc} and FF. The device performance improvement was achieved by
298 DFNM. Such a morphological scheme requires both high-quality D-A crystallites to form a
299 multi-length scaled dual fibril network, facilitating exciton diffusion and charge carrier transport.
300 This morphology also reduces the mixing zone content and feature size, from which exciton
301 splitting and carrier generation are more efficient. Meanwhile, the observation of NFA fibril-type
302 network crystallization is encouraging, which provides insights for the next generation material
303 design. Moreover, the synergetic combination of D18 and PM6 adds up the morphological and

photophysical advantages of the donor phase network to allow balanced exciton/free charge transport and recombination, contributing to the improvement of J_{sc} and FF. To sum up, the advantage of DFNM has been demonstrated, showing a bright future for its application in OSCs.

Acknowledgments

This work was financially supported by the National Natural Science Foundation of China (grant nos. 51973110, 21734009, 21905102, 51825301, 21734001 and 22109094), the National Key R&D Program of China (grant nos. 2020YFB1505500, 2020YFB1505502), the Program of Shanghai Science and Technology Commission science and technology innovation action plan (grant nos. 20ZR1426200, 20511103800, 20511103802 and 20511103803), the Natural Science Foundation of Shandong Province (grant no. ZR2019LFG005), the Key research project of Shandong Province (grant no. 2020CXGC010403), the Center of Hydrogen Science, Shanghai Jiao Tong University, China. J.N. and J.Y. thank the European Research Council for support under the European Union's Horizon 2020 research and innovation program (grant nos. 742708, 648901). We thank Cheng Wang and Chenhui Zhu from Advanced Light Source for providing X-ray scattering tests, which were carried out at beamline 7.3.3 and 11.0.1.2 at the Advanced Light Source, Molecular Foundry, Lawrence Berkeley National Laboratory, supported by the DOE, Office of Science, and Office of Basic Energy Sciences.

Author contributions

F.L. and Y.S. conceived and directed this project. L.Z. fabricated and characterized the OPV devices. L.Z. and M.Z. conducted the certification. J.X. processed and analyzed the single-crystal data. C.L. synthesized L8-BO. M.Z. and T.H. carried out the TPV, TPC, impedance characterization and analyzed the data. TA results and corresponding analysis were provided by G.Z. and H.Z. W.Z. carried out the GIXD and RSoXS measurement and assisted with data analysis.

J.S. conducted the AFM measurements. J.Y., R.C.M., and J.N. conduct the drift diffusion simulation and analysis. Yecheng Zou conducted the TEM measurements. Yongming Zhang, X.X., Z.Z., and R.Z. contributed to the fruitful discussion of this project. L.Z. and M.Z. wrote the manuscript and C.-C.C., J.Y., R.C.M., J.N., Y.S. and F.L. contributed to revisions of the manuscript. This manuscript was mainly prepared by F.L., Y.S., L.Z., M.Z. and J.X., and all authors participated in the manuscript preparation and commented on the manuscript.

Competing interests

The authors declare no competing interests.

Table 1 | Photovoltaic parameters of OSCs under the illumination of AM 1.5 G, 100 mW/cm^2.

Blends	Device Area (mm^2)	V_{oc} (V)	J_{sc} (mA cm^{-2})	FF (%)	PCE (%)
D18:L8-BO[a]	5.2[c]	0.907 (0.908 ± 0.001)	24.9 (24.3 ± 0.5)	78.5 (78.5 ± 1.0)	17.7 (17.4 ± 0.2)
	14.2[d]	0.907 (0.908 ± 0.001)	24.8 (24.2 ± 0.5)	77.6 (77.4 ± 1.3)	17.5 (17.1 ± 0.2)
PM6:L8-BO[a]	5.2[c]	0.888 (0.888 ± 0.001)	25.7 (25.5 ± 0.3)	79.9 (79.5 ± 1.1)	18.2 (18.0 ± 0.1)
	14.2[d]	0.888 (0.889 ± 0.001)	25.6 (25.6 ± 0.5)	78.8 (78.4 ± 1.4)	17.9 (17.6 ± 0.2)
PM6:D18:L8-BO[b]	5.2[c]	0.896 (0.896 ± 0.001)	26.7 (26.6 ± 0.3)	81.9 (81.1 ± 0.8)	19.6 (19.3 ± 0.1)
	14.2[d]	0.897 (0.897 ± 0.001)	26.7 (26.3 ± 0.4)	81.2 (80.4 ± 1.3)	19.4 (19.0 ± 0.2)
	5.2	0.891[e]	26.7[e]	80.8[e]	19.2[e]

[a]1:1.2 (weight ratio); [b]0.8:0.2:1.2 (weight ratio); [c]the average parameters were calculated from 50 devices, with an aperture area of 3.2 mm^2; [d]the average parameters were calculated from 20 devices, with an aperture area of 10.4 mm^2. The values outside the parentheses denote the best optimal photovoltaic parameters, and the values inside the parentheses represent the average photovoltaic parameters and their standard deviations. [e]Certified by National Photovoltaic Industry Metrology and Testing Center (NPVM), China. The designated illumination area was 3.084 mm^2.

Fig. 1 | Materials and device performance. Chemical structures (a) and energy level lineup (b) of PM6, D18, and L8-BO. (c) *J–V* curves of the devices based on D18:L8-BO, PM6:L8-BO, and PM6:D18:L8-BO (0.8:0.2:1.2) with a device area of 5.2 mm^2. (d) PCE, J_{sc}, and FF values of devices based on PM6:D18:L8-BO with different donor ratios. Error bars represent the standard error of the mean (n= 50). (e) EQE curves of the devices based on PM6:L8-BO, D18:L8-BO, and

PM6:D18:L8-BO. Inset is the change curves in EQE of the ternary device relative to the binary devices. (f) Histogram of PCE counts for 50 devices based on PM6:L8-BO, D18:L8-BO, and PM6:D18:L8-BO.

Fig. 2 | Morphology of thin films. (a) TEM image of PM6:L8-BO and PM6:D18:L8-BO blend films. (b) PiFM image at the wavenumber of 1532 cm^{-1} (representing L8-BO) and 1648 cm^{-1} (representing PM6) and the line profile to obtain the fibril width for PM6:D18:L8-BO blended film. The fibril width is in statistic from the full width at half maximum (the distance between the two adjacent dashed lines in the graph) (c) 2D GIXD patterns of PM6:L8-BO and PM6:D18:L8-BO blends. (d) In-plane (IP) and out-of-plane (OOP) line cut profiles of the 2D GIXD data based on binary and ternary blend films. (e) The scheme of DFNM with the charge transfer process. Robust fibrils in network surrounded by tiny ones. Such a hierarchical fibril network could form a good connection via chain segments with the mixing region, leading to a multi-length scaled morphology.

Fig. 3 | Device physics characterization. Carrier mobilities (a) and carrier diffusion length (b) of the binary and ternary devices (μ_e: electron mobility, μ_h: hole mobility, L_e: electron diffusion length, L_h: hole diffusion length). Error bars represent the standard error of the mean (n= 5). (c) The relationship between charge density and non-geminate recombination rate coefficient of the binary and ternary devices. The data points correspond to different light intensity and the filled symbol correspond to values at 1 sun intensity. (d) The derived occupied LUMO DoS from the capacitance spectra of the binary and ternary devices, exhibiting an exponential shape, where N is the total density per unit volume, and δ is the energetic disorder parameter.

Fig. 4 | Single-crystal structure of L8-BO and the scheme of DFNM. (a) The single twisted chain of L8-BO with three different dimer stacking modes. Each dimer is composed of two adjacent L8-BO. Top view (b) and side view (c) stacking diagram of three L8-BO twisted chains. (d) The optical micrographs of L8-BO single crystal. (e) Transmission electron microscopy (TEM) selected-area electron diffraction (SAED) patterns of L8-BO single crystal. The insert is the TEM bright-field (BF) image of L8-BO single crystal with labeled spindle axis direction. (f) The scheme of DFNM.

Fig. 5 | Exciton diffusion length and device parameters. (a) Exciton diffusion length in different acceptors ($PC_{61}BM$, $PC_{71}BM$, ITIC, IT4F, IDIC, Y6, BTP-eC9, and L8-BO). (b) Exciton diffusion length in different single or double blend donors (PM6, PM7, PTQ10, D18, D18-Cl, and PBT1-C-2Cl; PM6:D18=4:1, PM6:D18-Cl=4:1, PM6:PBT1-C-2Cl=4:1, PM7:D18=4:1, and PTQ10:D18=4:1). (c) Violin plots of PCE, FF, J_{sc}, and V_{oc} distribution of the binary (red) and ternary (blue) devices. System list: A: PM6:ITIC and PM6:D18:ITIC; B: PM6:IT4F and PM6:D18:IT4F; C: PM6:IDIC and PM6:D18:IDIC; D: PM6:IDTT-C10-TIC and PM6:D18:IDTT-C10-TIC; E: PM6:Y6 and PM6:D18:Y6; F: PM6:BTP-eC9 and PM6:D18:BTP-eC9; G: PM6:L8-BO and PM6:D18:L8-BO; H: PM7:Y6 and PM7:D18:Y6; I: PTQ10:Y6 and PTQ10:D18:Y6; J: PM7:L8-BO and PM7:D18:L8-BO; K: PTQ10:L8-BO and PTQ10:D18:L8-BO; L: PM6:Y6 and PM6:D18-Cl:Y6; M: PM6:Y6 and PM6:PBT1-C-2Cl:Y6; N:

PM6:L8-BO and PM6:D18-Cl:L8-BO; O: PM6:L8-BO and PM6:PBT1-C-2Cl:L8-BO. A-D: non-DFNM, E-O: DFNM. (*n*=50 for PM6:L8-BO, D18:L8-BO, and PM6:D18:L8BO, *n*=20 for the remaining conditions)

References

1 Li, G., Zhu, R. & Yang, Y. Polymer solar cells. *Nat. Photonics* **6**, 153-161, (2012).

2 Günes, S., Neugebauer, H. & Sariciftci, N. S. Conjugated Polymer-Based Organic Solar Cells. *Chem. Rev.* **107**, 1324-1338, (2007).

3 Yuan, J. *et al.* Single-Junction Organic Solar Cell with over 15% Efficiency Using Fused-Ring Acceptor with Electron-Deficient Core. *Joule* **3**, 1140-1151, (2019).

4 Zhang, M. *et al.* Single-layered organic photovoltaics with double cascading charge transport pathways: 18% efficiencies. *Nat. Commun.* **12**, 309, (2021).

5 Yang, F. & Forrest, S. R. Photocurrent Generation in Nanostructured Organic Solar Cells. *ACS Nano* **2**, 1022-1032, (2008).

6 Zhou, Z. *et al.* High-efficiency small-molecule ternary solar cells with a hierarchical morphology enabled by synergizing fullerene and non-fullerene acceptors. *Nat. Energy* **3**, 952-959, (2018).

7 Wang, Z. *et al.* The coupling and competition of crystallization and phase separation, correlating thermodynamics and kinetics in OPV morphology and performances. *Nat. Commun.* **12**, 332, (2021).

8 Zhu, L. *et al.* Progress and prospects of the morphology of non-fullerene acceptor based high-efficiency organic solar cells. *Energy Environ. Sci.* **14**, 4341-4357, (2021).

9 Lorch, C. *et al.* Controlling length-scales of the phase separation to optimize organic semiconductor blends. *Appl. Phys. Lett.* **107**, 201903, (2015).

10 Gasparini, N., Salleo, A., McCulloch, I. & Baran, D. The role of the third component in ternary organic solar cells. *Nat. Rev. Mater.* **4**, 229-242, (2019).

11 Lu, L., Kelly, M. A., You, W. & Yu, L. Status and prospects for ternary organic photovoltaics. *Nat. Photonics* **9**, 491-500, (2015).

12 Baran, D. *et al.* Reducing the efficiency–stability–cost gap of organic photovoltaics with highly efficient and stable small molecule acceptor ternary solar cells. *Nat. Mater.* **16**, 363-369, (2017).

13 Gasparini, N. *et al.* Designing ternary blend bulk heterojunction solar cells with reduced carrier recombination and a fill factor of 77%. *Nat. Energy* **1**, 16118, (2016).

14 Lu, L., Xu, T., Chen, W., Landry, E. S. & Yu, L. Ternary blend polymer solar cells with enhanced power conversion efficiency. *Nat. Photonics* **8**, 716-722, (2014).

15 Yang, Y. *et al.* High-performance multiple-donor bulk heterojunction solar cells. *Nat. Photonics* **9**, 190-198, (2015).

16 Kohn, P. *et al.* Crystallization-Induced 10-nm Structure Formation in P3HT/PCBM Blends. *Macromolecules* **46**, 4002-4013, (2013).

17 Sepe, A. *et al.* Structure formation in P3HT/F8TBT blends. *Energy Environ. Sci.* **7**, 1725-1736, (2014).

18 Kirchartz, T., Agostinelli, T., Campoy-Quiles, M., Gong, W. & Nelson, J. Understanding the Thickness-Dependent Performance of Organic Bulk Heterojunction Solar Cells: The Influence of Mobility, Lifetime, and Space Charge. *J. Phys. Chem. Lett.* **3**, 3470-3475, (2012).

19 Kirchartz, T., Bisquert, J., Mora-Sero, I. & Garcia-Belmonte, G. Classification of solar cells according to mechanisms of charge separation and charge collection. *Phys. Chem. Chem. Phys.* **17**, 4007-4014, (2015).

20 Li, C. *et al.* Non-fullerene acceptors with branched side chains and improved molecular packing to exceed 18% efficiency in organic solar cells. *Nat. Energy* **6**, 605-613, (2021).

21 Zahn, D. R. T., Gavrila, G. N. & Gorgoi, M. The transport gap of organic semiconductors studied using the combination of direct and inverse photoemission. *Chem. Phys.* **325**, 99-112, (2006).

22 Zhang, M. *et al.* High-Efficiency Organic Photovoltaics using Eutectic Acceptor Fibrils to Achieve Current Amplification. *Adv. Mater.* **33**, 2007177, (2021).

23 Song, J. *et al.* High-efficiency organic solar cells with low voltage loss induced by solvent additive strategy. *Matter* **4**, 2542-2552, (2021).

24 Cui, Y. *et al.* Single-Junction Organic Photovoltaic Cell with 19% Efficiency. *Adv. Mater.* **33**, 2102420, (2021).

25 Chong, K. *et al.* Realizing 19.05% Efficiency Polymer Solar Cells by Progressively Improving Charge Extraction and Suppressing Charge Recombination. *Adv. Mater.* **34**, 2109516, (2022).

26 Liu, Q. *et al.* 18% Efficiency organic solar cells. *Sci. Bull.* **65**, 272-275, (2020).

27 Song, J. *et al.* Morphology Characterization of Bulk Heterojunction Solar Cells. *Small Methods* **2**, 1700229, (2018).

28 Sangroniz, L., Cavallo, D. & Müller, A. J. Self-Nucleation Effects on Polymer Crystallization. *Macromolecules* **53**, 4581-4604, (2020).

29 Oh, J. Y. *et al.* Self-Seeded Growth of Poly(3-hexylthiophene) (P3HT) Nanofibrils by a Cycle of Cooling and Heating in Solutions. *Macromolecules* **45**, 7504-7513, (2012).

30 Liu, F., Brady, M. A. & Wang, C. Resonant soft X-ray scattering for polymer materials. *Eur. Polym. J.* **81**, 555-568, (2016).

31 Wang, C. *et al.* Defining the Nanostructured Morphology of Triblock Copolymers Using Resonant Soft X-ray Scattering. *Nano Lett.* **11**, 3906-3911, (2011).

32 Su, G. M., Patel, S. N., Pemmaraju, C. D., Prendergast, D. & Chabinyc, M. L. First-Principles Predictions of Near-Edge X-ray Absorption Fine Structure Spectra of Semiconducting Polymers. *J. Phys. Chem. C* **121**, 9142-9152, (2017).

33 Watts, B., Swaraj, S., Nordlund, D., Lüning, J. & Ade, H. Calibrated NEXAFS spectra of common conjugated polymers. *J. Chem. Phys.* **134**, 024702, (2011).

34 Zhong, W. *et al.* Decoupling Complex Multi-Length-Scale Morphology in Non-Fullerene Photovoltaics with Nitrogen K-Edge Resonant Soft X-Ray Scattering. *Adv. Mater.* **34**, 2107316, (2021).

35 Collins, B. A. *et al.* Polarized X-ray scattering reveals non-crystalline orientational ordering in organic films. *Nat. Mater.* **11**, 536-543, (2012).

36 Liu, F. *et al.* Relating Chemical Structure to Device Performance via Morphology Control in Diketopyrrolopyrrole-Based Low Band Gap Polymers. *J. Am. Chem. Soc.* **135**, 19248-19259, (2013).

37 Bakulin, A. A. *et al.* The Role of Driving Energy and Delocalized States for Charge Separation in Organic Semiconductors. *Science* **335**, 1340-1344, (2012).

38 Rao, A. *et al.* The role of spin in the kinetic control of recombination in organic photovoltaics. *Nature* **500**, 435-439, (2013).

39 Sandberg, O. J., Tvingstedt, K., Meredith, P. & Armin, A. Theoretical Perspective on Transient Photovoltage and Charge Extraction Techniques. *J. Phys. Chem. C* **123**, 14261-14271, (2019).

40 MacKenzie, R. C. I., Shuttle, C. G., Chabinyc, M. L. & Nelson, J. Extracting Microscopic Device Parameters from Transient Photocurrent Measurements of P3HT:PCBM Solar Cells. *Adv. Energy Mater.* **2**, 662-669, (2012).

41 Xiao, B. *et al.* Relationship between Fill Factor and Light Intensity in Solar Cells Based on Organic Disordered Semiconductors: The Role of Tail States. *Phys. Rev. Appl.* **14**, 024034, (2020).

42 MacKenzie, R. C. I., General-purpose Photovoltaic Device Model–gpvdm, https://www.gpvdm.com

43 Wang, C., Dong, H., Jiang, L. & Hu, W. Organic semiconductor crystals. *Chem. Soc. Rev.* **47**, 422-500, (2018).

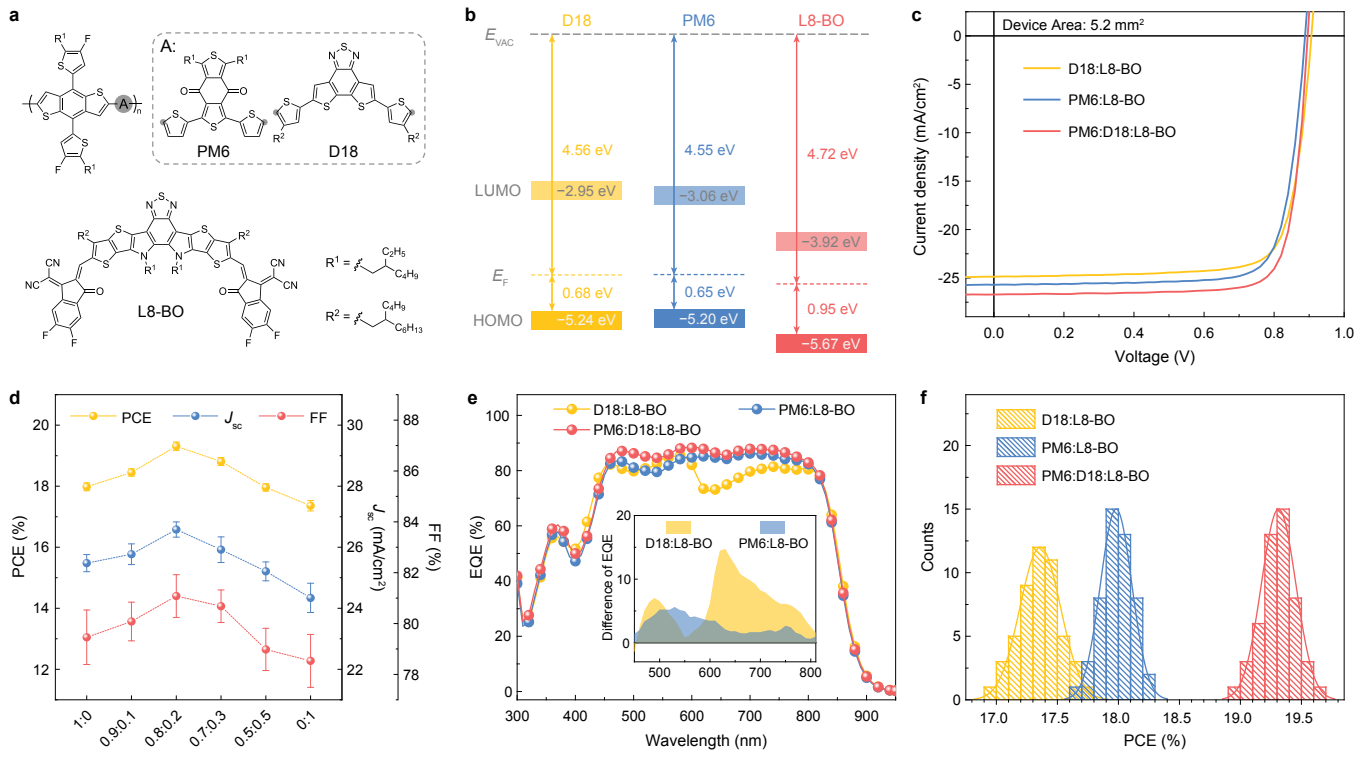
44 Lai, H. & He, F. Crystal Engineering in Organic Photovoltaic Acceptors: A 3D Network Approach. *Adv. Energy Mater.* **10**, 2002678, (2020).

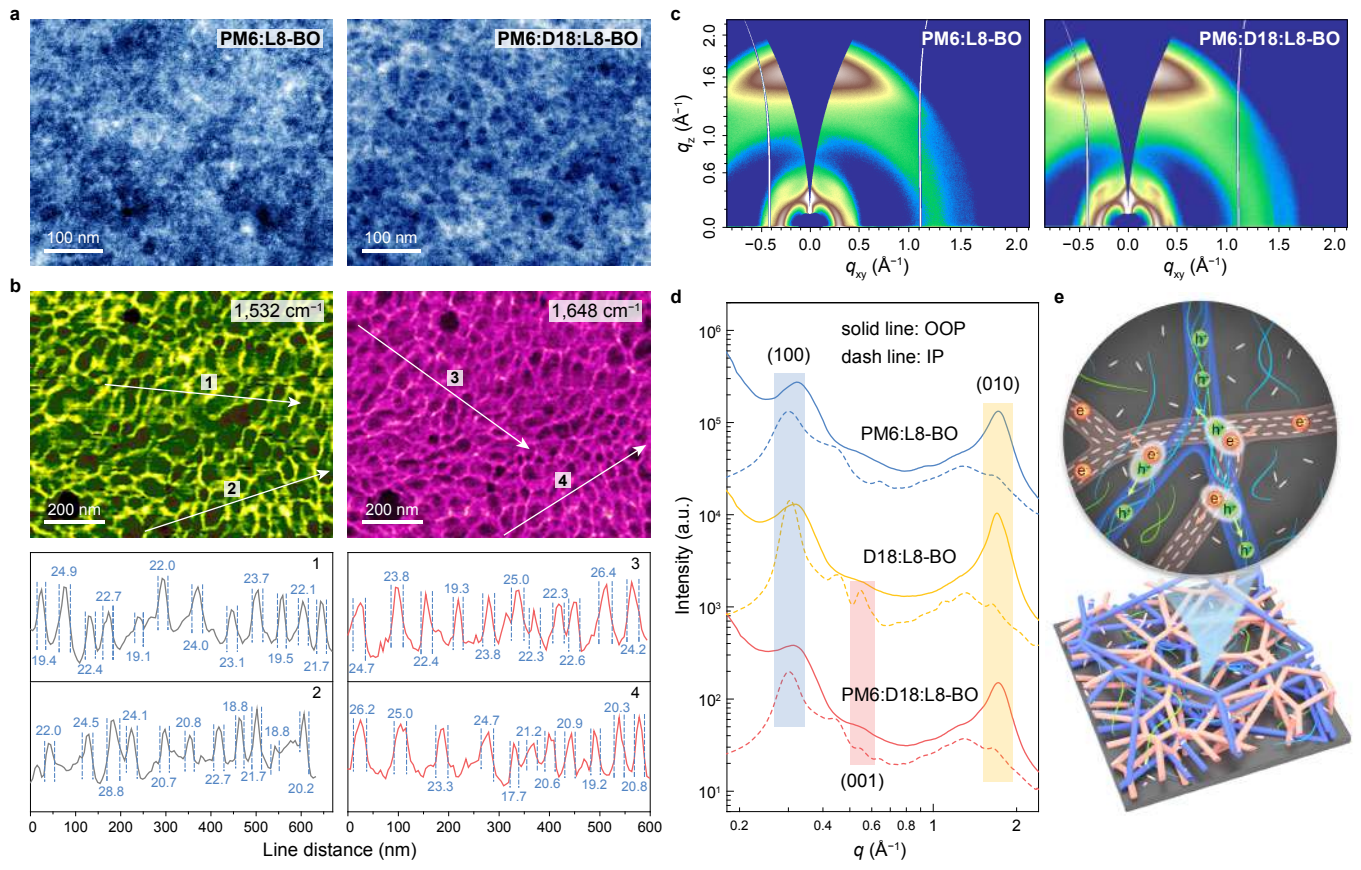
45 Zhu, L. *et al.* Efficient Organic Solar Cell with 16.88% Efficiency Enabled by Refined Acceptor Crystallization and Morphology with Improved Charge Transfer and Transport Properties. *Adv. Energy Mater.* **10**, 1904234, (2020).

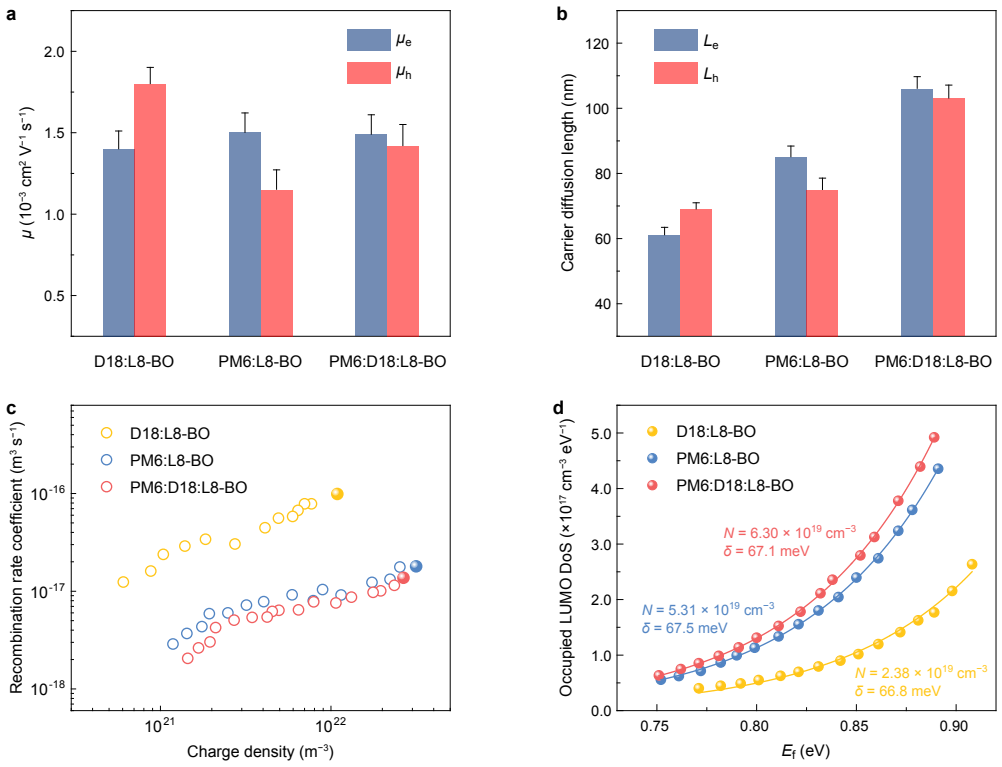
Methods

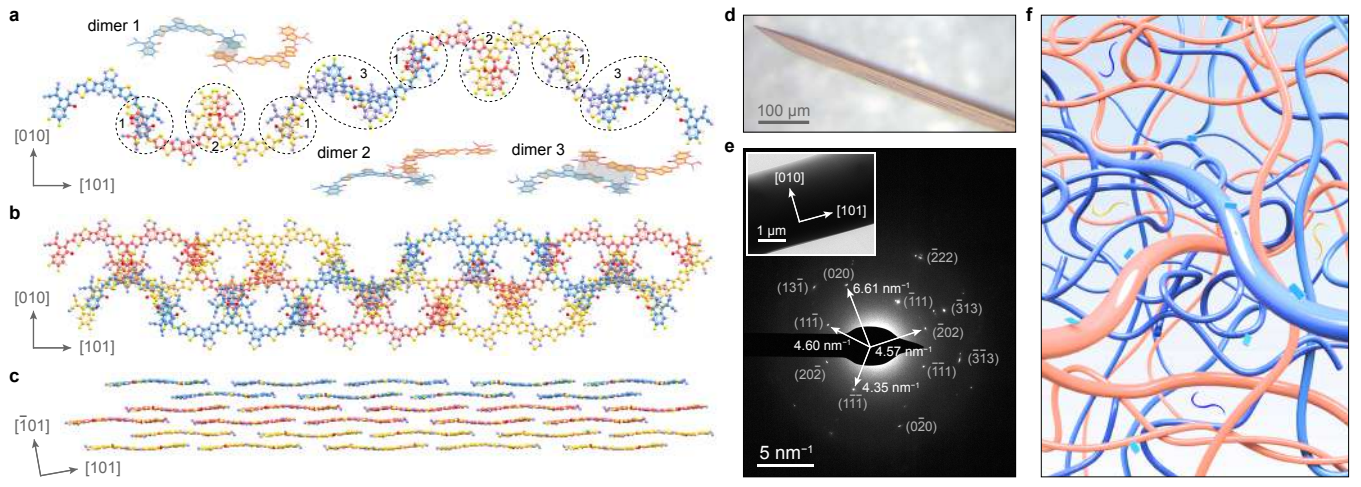
Device Fabrication. Organic solar cell devices with indium tin oxide (ITO) /poly(3,4-ethylenedioxythiophene):poly(styrene sulfonate) (PEDOT:PSS)/active layer/PNDIT-F3N/Ag structures were fabricated according to the following procedure. Patterned ITO glass substrates were sequential cleaned by ultrasonication in detergent, deionized water, acetone, and isopropyl alcohol for 20 min each and then dried under a dry oven. The precleaned substrates were treated in an ultraviolet-ozone chamber for 15 min, then a ~20 nm thick PEDOT:PSS (Clevious P VP AI 4083 H. C. Stark, Germany) thin film was deposited onto the ITO surface by spin-coating and baked at 150 °C for 15 min. The solution of PM6:L8-BO (1:1.2, wt., 14.3 mg mL^{-1} in total), D18:L8-BO (1:1.2, wt., 13.2 mg mL^{-1} in total), and PM6:D18:L8-BO

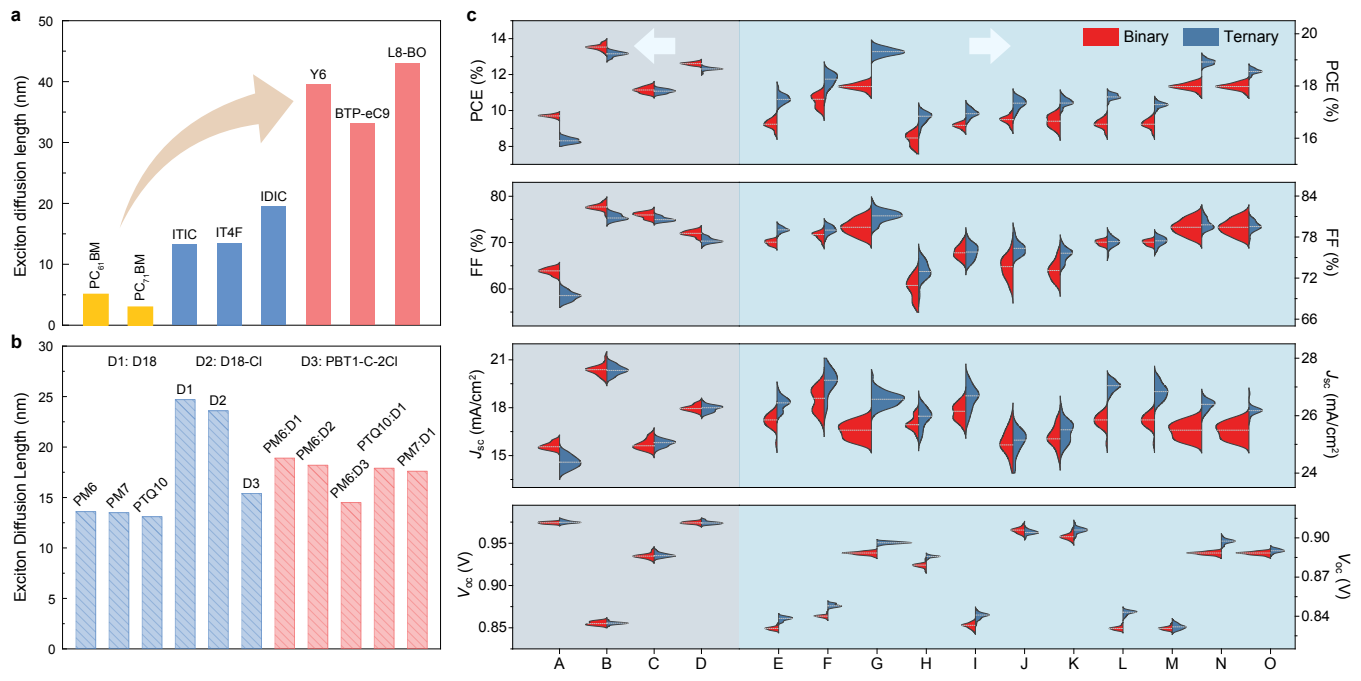
493 (0.8:0.2:1.2, wt., 14.3 mg mL^{-1} in total) in chloroform with 1,4-diiodobenzene (DIB) as a solid
494 additive (the content of DIB is 50% of the total mass of donor and acceptor) was stirred at 25 °C
495 for 2 hours in advance and then spin-coated on top of the PEDOT:PSS layer. The optimum
496 thickness of the active layer is 120 nm (statistical variations within 5 nm). The prepared films were
497 treated with thermal annealing at 85 °C for 5 min. After cooling to room temperature, a ~5 nm
498 thick of PNDIT-F3N (0.5 mg mL^{-1} in methanol with 0.5% acetic acid, v/v) was spin-coated on the
499 top of the active layer. Then, those samples were brought into an evaporating chamber and a 150
500 nm thick silver layer was thermally evaporated on the PNDIT-F3N layer at a base pressure of $1 \times$
501 10^{-6} mbar. The evaporation thickness was controlled by SQC-310C deposition controller
502 (INFICON, Germany). Ten devices were fabricated on one substrate and the active area of each
503 device was 0.052 cm^2 defined by a shadow mask.


a
A:
PM6
D18
L8-BO
R1 = C2H5 C4H9
R2 = C4H9 C6H13
b
D18
PM6
L8-BO
EVAC
4.56 eV
4.55 eV
4.72 eV
LUMO
−2.95 eV
−3.06 eV
−3.92 eV
EF
0.68 eV
0.65 eV
0.95 eV
HOMO
−5.24 eV
−5.20 eV
−5.67 eV
c
Device Area: 5.2 mm2
D18:L8-BO
PM6:L8-BO
PM6:D18:L8-BO
Current density (mA/cm2)
Voltage (V)
d
PCE
Jsc
FF
PCE (%)
Jsc (mA/cm2)
FF (%)
1:0
0.9:0.1
0.8:0.2
0.7:0.3
0.5:0.5
0:1
e
D18:L8-BO
PM6:L8-BO
PM6:D18:L8-BO
EQE (%)
Wavelength (nm)
Difference of EQE
f
D18:L8-BO
PM6:L8-BO
PM6:D18:L8-BO
Counts
PCE (%)


a
PM6:L8-BO
PM6:D18:L8-BO
100 nm
100 nm
b
1,532 cm⁻¹
1,648 cm⁻¹
1
2
3
4
200 nm
200 nm
24.9
22.0
22.7
23.7
22.1
19.4
22.4
19.1
24.0
23.1
19.5
21.7
23.8
19.3
25.0
22.3
26.4
24.7
22.4
23.8
22.3
22.6
24.2
22.0
24.5
24.1
20.8
18.8
18.8
28.8
20.7
22.7
21.7
20.2
26.2
25.0
24.7
21.2
20.9
20.3
23.3
17.7
20.6
19.2
20.8
0 100 200 300 400 500 600
Line distance (nm)
c
PM6:L8-BO
PM6:D18:L8-BO
q_z (Å^{-1})
q_{xy} (Å^{-1})
d
solid line: OOP
dash line: IP
(100)
(010)
(001)
PM6:L8-BO
D18:L8-BO
PM6:D18:L8-BO
Intensity (a.u.)
q (Å^{-1})
e
h⁺
e⁻


a
μ (10^{-3} cm^2 V^{-1} s^{-1})
2.0
1.5
1.0
0.5
μ_e
μ_h
D18:L8-BO
PM6:L8-BO
PM6:D18:L8-BO
b
Carrier diffusion length (nm)
120
100
80
60
40
L_e
L_h
D18:L8-BO
PM6:L8-BO
PM6:D18:L8-BO
c
Recombination rate coefficient (m^3 s^{-1})
10^{-16}
10^{-17}
10^{-18}
D18:L8-BO
PM6:L8-BO
PM6:D18:L8-BO
10^{21}
10^{22}
Charge density (m^{-3})
d
Occupied LUMO DoS (×10^{17} cm^{-3} eV^{-1})
5.0
4.0
3.0
2.0
1.0
0.0
D18:L8-BO
PM6:L8-BO
PM6:D18:L8-BO
N = 6.30 × 10^{19} cm^{-3}
δ = 67.1 meV
N = 5.31 × 10^{19} cm^{-3}
δ = 67.5 meV
N = 2.38 × 10^{19} cm^{-3}
δ = 66.8 meV
0.75
0.80
0.85
0.90
E_f (eV)


a
dimer 1
dimer 2
dimer 3
1
2
3
[010]
[101]
b
[010]
[101]
c
[$\bar{1}$01]
[101]
d
100 μm
e
[010]
[101]
1 μm
(020)
(13$\bar{1}$)
6.61 nm^{-1}
(11$\bar{1}$)
4.60 nm^{-1}
4.57 nm^{-1}
(20$\bar{2}$)
4.35 nm^{-1}
(11$\bar{1}$)
(0$\bar{2}$0)
(222)
(1$\bar{1}$1)
(3$\bar{1}$3)
(202)
(3$\bar{1}$3)
(1$\bar{1}$1)
5 nm^{-1}
f


a
Exciton diffusion length (nm)
PC61BM
PC71BM
ITIC
IT4F
IDIC
Y6
BTP-eC9
L8-BO
b
Exciton Diffusion Length (nm)
D1: D18
D2: D18-Cl
D3: PBT1-C-2Cl
PM6
PM7
PTQ10
D1
D2
D3
PM6:D1
PM6:D2
PM6:D3
PTQ10:D1
PM7:D1
c
Binary
Ternary
PCE (%)
FF (%)
Jsc (mA/cm2)
Voc (V)
A
B
C
D
E
F
G
H
I
J
K
L
M
N
O